

Ab initio approach to structural, electronic, and ferroelectric properties of antimony sulphoiodideDanila Amoroso^{1,*} and Silvia Picozzi²¹*Università degli Studi di L'Aquila, Dip. Scienze Fisiche e Chimiche, 67100 L'Aquila, Italy*²*Consiglio Nazionale delle Ricerche, Istituto SPIN, UOS L'Aquila, Sede di lavoro CNR-SPIN c/o Univ. "G. D'Annunzio", 66100 Chieti, Italy*

(Received 18 February 2016; revised manuscript received 13 May 2016; published 10 June 2016)

By means of first-principles calculations for the SbSI semiconductor, we show that bare density functional theory fails to reproduce the experimentally observed ferroelectric phase, whereas a more advanced approach, based on hybrid functionals, correctly works. When comparing the paraelectric and ferroelectric phases, our results show polar displacements along the c direction of the Sb and S sublattices with respect to the iodine framework, leading to a predicted spontaneous polarization of $P \simeq 20 \mu\text{C}/\text{cm}^2$, in good agreement with experiments. In the ferroelectric phase, the semiconducting behavior of SbSI is confirmed by relatively large values for the indirect and direct gaps ($\simeq 2.15$ eV and 2.3 eV, respectively). An analysis of the electronic structure, in terms of density of states, charge density distribution, and anomalies in the Born effective charges, reveals (i) the clear presence of a Sb(III) lone pair and (ii) a large covalency in the SbSI bonding, based on the hybridization between Sb and S ions, in turn more ionically bonded to iodine anions. Finally, the interplay between ferroelectricity and spin-orbit coupling reveals a coexistence of Dresselhaus and Rashba relativistic effects and a spin texture that can be reversed by switching the polarization, of potential appeal in electrically controlled spintronics.

DOI: [10.1103/PhysRevB.93.214106](https://doi.org/10.1103/PhysRevB.93.214106)**I. INTRODUCTION**

Multifunctional materials, i.e., compounds with two or more (possibly coupled) functionalities, often lie at the heart of revolutions in condensed matter physics, both from the basic and technological points of view, as recently shown by multiferroics or diluted magnetic semiconductors. In this framework, our work addresses a new class of multifunctional materials: ferroelectrics [1] with large relativistic spin-orbit coupling and Rashba effects [2,3], which are briefly introduced below.

Insulating systems that exhibit spontaneous macroscopic polarization \mathbf{P} , switchable by an applied electric field, are classified as ferroelectric (FE) materials [1], showing a wide range of technological applications, ranging from nonvolatile random-access memory to ultrasonic imaging, from optical devices to energy harvesting and production. In particular, ferroelectrics are believed to be relevant in photovoltaics, as the electric field can help to separate electron-hole pairs created in FE, therefore increasing the photocurrent and leading to a larger solar cell efficiency [4,5]. The so-called “bulk photovoltaic” effect is also at the center of increasing interests in many ferroelectric materials [4]. Within spintronics phenomena, the Rashba effect, in which the spin degeneracy is removed as a consequence of the joint action of atomic spin-orbit coupling (SOC) and asymmetry of the crystal field potential, plays a leading role in devices based on spin-polarized currents or spin injection [2,3,6]. While k -dependent spin splitting phenomena in three-dimensional solids as arising from bulk inversion asymmetry were generally described in terms of the Dresselhaus effect [7], only recently Rashba effects have been discovered in bulk materials [8,9]. It was also suggested that Rashba and Dresselhaus effects can coexist

and the observed spin splitting can be classified on the basis of atomic site point group lacking inversion symmetry, rather than from the acentricity of the crystal space group [10].

The main idea behind ferroelectric Rashba semiconductors (FERSC) [11] is to combine SOC with ferroelectricity to achieve new multifunctional materials where, thanks to a (possibly large) Rashba/Dresselhaus spin splitting, the spin texture is controllable and switchable via an electric field. A few prototypical materials (tellurides, such as GeTe [9], SnTe [12], alloys [13], organic-inorganic halides [5,14,15], or hyperferroelectrics [16]) were reported in the literature so far, but the field needs to be consolidated via the study of additional relativistic ferroelectrics with optimized performances. Our approach towards the design of novel relativistic ferroelectrics has been primarily driven by the presence of (i) heavy elements (i.e., high SOC) and (2) robust ferroelectricity, persistent at high temperature and with large polarization. Within this context, an overlooked class of ferroic materials is represented by antimony chalcogenides. In closer detail, antimony sulfur iodide (SbSI) shows semiconducting properties, high photoconductivity [17], ferroelectricity [18], piezoelectricity [19], and nonlinear optical behavior [20]. The first investigation of photoelectric properties of single crystals of the ternaries V-VI-VII (V = Sb, Bi; VI = S, Se, Te; VII = Cl, Br, I) dates back to 1959 by Nietsche and Merz [17]. They have reported that in SbSI the wavelength of maximum photocurrent is $\lambda_{\text{max}} \simeq 6300\text{--}6400 \text{ \AA}$, i.e., the optical band gap amounts to ~ 2 eV. The discovery of ferroelectricity in SbSI goes back to Fatuzzo *et al.* in 1962 [18]; measurements of the dielectric constant and of the hysteresis loop showed that SbSI is a ferroelectric with a Curie temperature $T_c \sim 22^\circ\text{C}$ and a high spontaneous polarization $P_s = 25 \mu\text{C}/\text{cm}^2$ at 0°C [18]. Audzijonis *et al.* [21,22] also proposed the existence of a high temperature antiferroelectric phase transition in the phase diagram of SbSI, in the temperature region $298 < T_c < 410 \text{ K}$.

Despite SbSI being known for many years, its theoretical characterization is rather poor, and few nonexhaustive *ab initio* studies exist in the literature. For example, within a framework

*Present address: Physique Théorique des Matériaux, Université de Liège (B5), B-4000 Liège, Belgium; CNRS, Université de Bordeaux, ICMCB, UPR 9048, F-33600 Pessac, France.

of a broader review on photoferroics, Butler *et al.* [23] briefly discussed the electronic and FE properties of SbSI, SbSeI, and SbSBr [24].

In this work, we present a comprehensive first-principles analysis of SbSI. In closer detail, after reporting some technicalities in Sec. II, we focus on the structural (Sec. III), electronic (Sec. IV), and ferroelectric properties (Sec. V). Due to the presence of heavy elements and the low-symmetric FE ground state in antimony sulphoiodide, we explored the additional effects led by SOC in Sec. VI and reported our conclusions in Sec. VII.

II. COMPUTATIONAL DETAILS

Ab initio calculations within the density functional theory (DFT) on SbSI were performed using the projector-augmented wave methods implemented in the VASP code [25,26]. To describe the exchange-correlation (xc) potential, we employed the Perdew-Burke-Ernzerhof (PBE) [27] functional within the generalized gradient approximation (GGA) for all simulations. Furthermore, to overcome failures of standard DFT in reproducing the SbSI structural properties (see below), we used the Heyd-Scuseria-Ernzerhof (HSE) hybrid density functional approach [28]. In order to analyze the relativistic effects on band structures and on ferroelectricity, SOC has been also included. Good convergence for the bulk total energy calculation has been achieved with the choice of the energy cutoff at 400 eV both for the PBE and HSE functionals, applying, for the Brillouin zone sampling, a Monkhorst-Pack mesh grid $5 \times 4 \times 8$ and $4 \times 4 \times 8$, respectively. For Sb and I atoms, $5s$ and $5p$ electrons, and for S, $3s$ and $3p$ electrons were considered as valence electrons. Atomic positions were optimized until the residual forces were smaller than $0.001 \text{ eV \AA}^{-1}$. Test calculations related to the ionic relaxation were performed using the local-density approximation (LDA) [29] and van der Waals correction within the so-called Grimme D2 approach [30]. The calculation of the macroscopic polarization by means of the Berry phase [31] was performed on the relaxed structure by using both PBE and nonlocal HSE functionals.

III. STRUCTURAL DETAILS

SbSI in both paraelectric and ferroelectric phases is orthorhombic and has four SbSI molecules (12 atoms) per unit cell [32], as shown in Table I and Fig. 1. The space group is $D_{2h}^{16} - Pnam$ in the paraelectric phase above the Curie temperature ($T_c > 298 \text{ K}$) and $C_{2v}^9 - Pna2_1$ in the ferroelectric phase below the Curie temperature ($T_c < 298 \text{ K}$). According to the x-ray experimental structure [33] for the nonpolar state of SbSI, the atoms are grouped in parallel layers in the x - y plane and extend in a chainlike form along the c axis (which is also the polarization direction). It was suggested [34–36] that the interaction between two double chains of SbSI

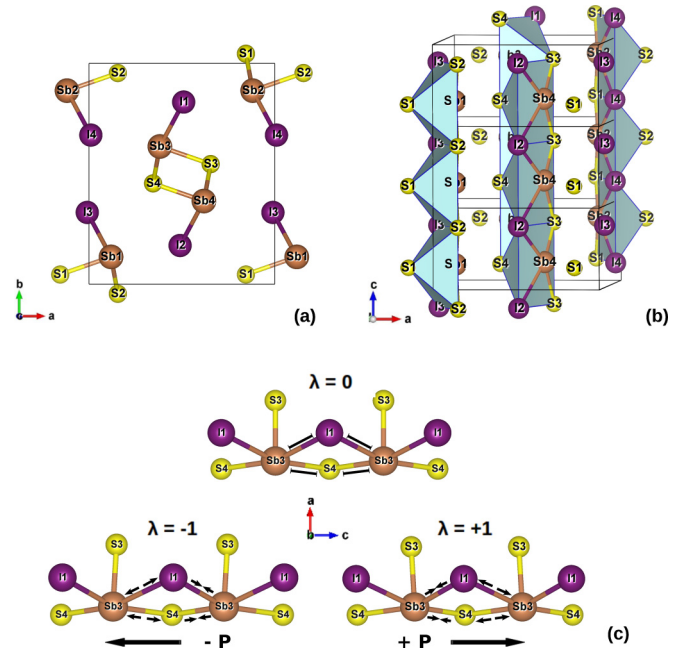


FIG. 1. Schematic representation of SbSI. (a) Atomic positions in the x - y plane in the crystalline unit cell. (b) SbSI crystal highlighting both the rhombic-bipyramidal atomic arrangement, as well as a quasi-one-dimensional structure composed of zigzag chains of $[Sb_2S_4I_4]_n$ dimers stacked along the crystallographic c axis. (c) Zoom over relevant ions: double arrows show the switching between shorter and longer bond lengths in the FE state, according to the polar mode amplitude $\lambda = \pm 1$, compared with those in the PE phase $\lambda = 0$. The polarization direction is also reported.

crystal is negligible, i.e., chains of atoms parallel to the z axis are linked only via a weak van der Waals-type interaction. This “one-double-chain” (or “single-double-chain”) model characterizes the simplified unit cell (SUC), containing only two SbSI molecular units. The C_{2h}^2 SUC is obtained from the central group of Sb_3 - Sb_4 - S_3 - S_4 - I_1 - I_2 atoms [cf. Figs. 1(a) and 1(b)], which form the chainlike ensemble along the c direction. The SbSI crystal can also be alternatively visualized as a quasi-one-dimensional structure composed of zigzag chains of $[Sb_2S_4I_4]_n$ dimers stacked along the crystallographic c direction, like rhombic-bipyramidal system, as shown in Fig. 1(b).

Within the framework where I site is kept fixed, in line with the experimental characterization of the crystal [32,34,37], the FE structure is characterized by cooperative displacements of Sb and S with respect to iodine along the polarization direction [see Fig. 1(c)]. The predominant role is played by the large movement of antimony atoms from high-symmetry positions. The polarity of the double chains results from the asymmetry of (S, I)-Sb arrangement due to alternating shorter and longer Sb-S and Sb-I bonds; these displacements are all oriented in the same direction along the z axis, leading to a net FE polarization.

For SbSI, we have studied the structural properties within and beyond the local density approximation, and we have compared our results with those obtained from x-ray diffraction analysis by Kikuchi *et al.* [32] at 35°C for the paraelectric phase and at 5°C for the ferroelectric phase.

TABLE I. Locations of the four molecules in the $Pna2_1$ unit cell.

$(SbSI)_1 = (x, y, z)$	$(SbSI)_2 = (-x, -y, \frac{1}{2} + z)$
$(SbSI)_3 = (\frac{1}{2} - x, \frac{1}{2} + y, \frac{1}{2} + z)$	$(SbSI)_4 = (\frac{1}{2} + x, \frac{1}{2} - y, z)$

TABLE II. Relaxed atomic positions obtained within pure GGA (PBE), PBE with Grimme’s D2 correction (PBE-vdW), and HSE functionals, starting from the *Pna2₁* symmetry. Experimental values from x-ray diffraction [32] are also reported.

Atoms		PBE	PBE-vdW	HSE	Expt. (5 °C)
Sb	<i>x</i>	0.121	0.127	0.119	0.119
	<i>y</i>	0.124	0.120	0.124	0.123
	<i>z</i>	0.270	0.270	0.295	0.298
S	<i>x</i>	0.843	0.845	0.845	0.843
	<i>y</i>	0.045	0.049	0.044	0.049
	<i>z</i>	0.270	0.270	0.263	0.261
I	<i>x</i>	0.509	0.496	0.510	0.508
	<i>y</i>	0.827	0.828	0.825	0.828
	<i>z</i>	0.270	0.270	0.251	0.250

As the crystalline phase is based on double-chains’ weak interactions—well known to be not correctly reproduced within standard DFT—we decided to keep the experimental lattice constants [33] for all calculations: $a = 8.49 \text{ \AA}$, $b = 10.10 \text{ \AA}$, and $c = 4.16 \text{ \AA}$. We tested, however, that the main results do not qualitatively change if the Bravais vectors are chosen in agreement with other literature studies. A direct comparison with a previous *ab initio* study by Butler *et al.* [23] could not be performed, as computational parameters were not fully detailed and no internal atomic positions were reported there.

In Table II we report the atomic positions as obtained by *ab initio* relaxations using bare PBE and HSE. It is evident that standard DFT leads to the same *z*-coordinates for Sb, S, and I, i.e., the atomic displacements are canceled along the *c* direction leading to the nonpolar phase as the stable one [38]. As a result, all LDA and PBE exchange-correlation functionals fail to reproduce the experimentally observed ferroelectric phase. On the other hand, the improvements carried by the hybrid functional (HSE) in the ferroelectric structural optimization are remarkable. As shown in both Tables II and III, HSE well reproduces the relevant structural parameters of SbSI; in fact, the bond lengths are consistent with experimental data within 1% and the Sb and S displacements with respect to I kept fixed, are about $\tau_{Sb} = 0.18 \text{ \AA}$ and $\tau_S = 0.05 \text{ \AA}$, in excellent agreement with experiments. Moreover, the ferroelectric state is lower in energy than the paraelectric phase (by -6 meV per unit cell; -1.5 meV per f.u.), which proves the stability of the low symmetry phase (see also below).

We note that the stability of ferroelectric vs paraelectric phase has been tested as a function of the computational parameters (such as cutoff energy and *k*-meshes) and structural parameters (such as volume and lattice constants). In all the tested cases, PBE always led to a paraelectric ground state. We remark that the stability of ferroelectricity with respect to paraelectricity is a very delicate quantity, depending on the subtle balance between competing energy terms favoring or not the ferroelectric distortion (see Ref. [1] and references therein). Our results show that, despite its higher computational cost, the HSE hybrid functional, by slightly changing the electronic structure obtained via local xc potentials, is the only exchange-correlation approach capable of reproducing the FE phase transition and of providing a better description of the SbSI

TABLE III. Comparison between theoretical and experimental bond lengths. Bonds’ notation in the first column is consistent with Fig. 1. Different values for some bonds in the FE phase are due to the shorter and longer links caused by the Sb and S displacements along the polarization *c* direction.

Bonds	PE phase		FE phase	
	HSE	Expt. (35 °C)	HSE	Expt. (5 °C)
$Sb_3 - S_4$	2.692	2.746	2.801	2.835
			2.596	2.605
$Sb_3 - S_3$	2.461	2.492	2.464	2.475
$Sb_3 - I_1$	3.097	3.098	3.231	3.247
			2.987	2.987
$Sb_3 - I_4$	3.823	3.813	3.918	3.926
			3.719	3.714
$S_3 - S_4$	3.461	3.551	3.469	3.516
$S_4 - I_1$	3.956	4.084	3.976	4.071
$S_4 - I_2$	3.733	3.713	3.703	3.691
			3.758	3.741
$S_4 - I_4$	3.612	3.620	3.605	3.631
$S_4 - I'_3$	3.894	3.815	3.866	3.812
			3.919	3.860
$I_1 - I_4$	4.501	4.546	4.506	4.548
$I_1 - I'_2$	4.121	4.052	4.107	4.043

system’s structural properties. However, as we will show below, once the atomic positions are fixed to those predicted by HSE, the PBE still provides a good description of the ferroelectric and electronic properties.

IV. ELECTRONIC PROPERTIES

Let’s now analyze the density of states and the band structures, focusing on the effects of exchange-correlation functionals and of atomic arrangements within the crystal. By examining the total DOS [cf. Fig. 2(c)] and thanks to the orbitally and atomically resolved DOS (not shown in the lowest energy range), we note that states deriving from the *3s* orbital of sulfur and *5s* of iodine are strongly localized in the deeper valence region, (i.e., $[-14.5 : -13] \text{ eV}$ within HSE), whereas the *5s* level of antimony is closer to the upper part of the valence band, i.e., $[-10 : -7] \text{ eV}$ within HSE. Moreover, the valence states in the energy range $[-5 : 0] \text{ eV}$ within HSE are mostly composed by I *5p* and S *3p* orbitals, although a relevant contribution from the Sb *5p* orbitals is also present, as shown in Fig. 2(a). The conduction band is mainly formed by Sb *p*, I *p* orbitals, and S *p* [cf. Fig. 2(b)]. In Fig. 2(c), we see that the DOS within standard DFT does not show any relevant differences when compared to HSE, except for an expected increase in the band gap (by less than a few percent).

As shown in the (HSE with SOC) band structure reported in Fig. 3(a), the SbSI crystal has an indirect forbidden energy gap both in the paraelectric and in the ferroelectric phases: the minimum of the conduction band (CBM) is located at the *S* point of the Brillouin zone and the maximum of the valence band (VBM) is located at the *T* point. Moreover, a visible direct gap exists along the $\Gamma - Y$ line in the first Brillouin zone in both phases. Within PBE, in the ferroelectric structure the value of the indirect gap ($T \rightarrow S$) amounts to 1.60 eV and

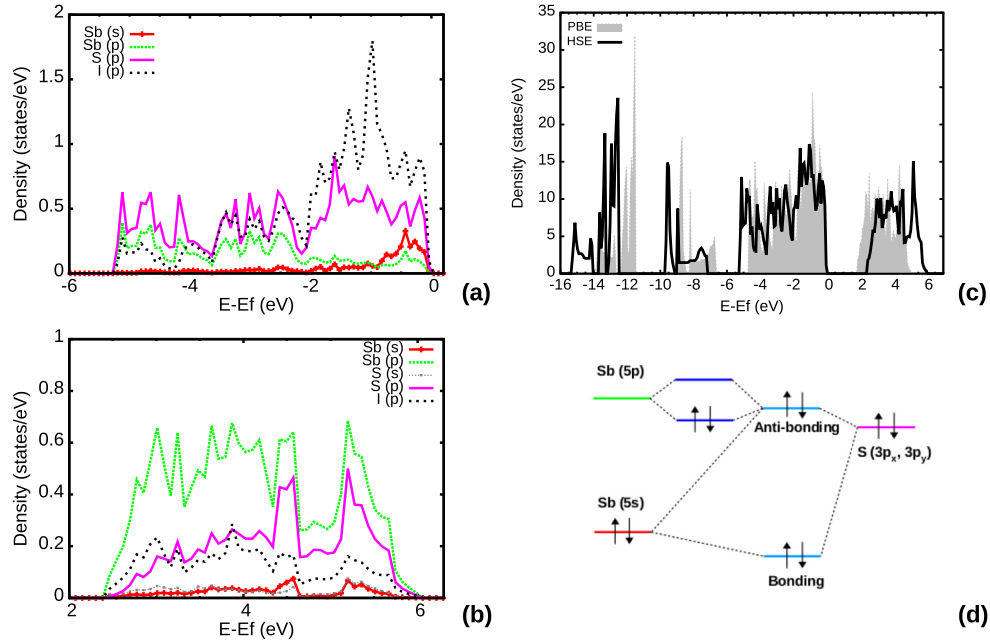


FIG. 2. Partial density of states in the ferroelectric phase: in (a) valence band $[-5.3 : 0]$ eV and (b) conduction band $[2.5 : 6]$ eV. Contribution from each type of atom and orbital is reported in different colored lines. (c) Comparison between total DOS in PBE and in HSE. (d) Illustration of the orbital interactions diagram that lead to Sb lone pair formation and interaction with “nominally” empty Sb $5p$ states: first interaction between Sb($5s$) and S($3p$) (both filled); second interaction between antibonding states and (empty) Sb($5p$) levels.

it decreases to 1.54 eV in the paraelectric structure. The direct band gap ($\Gamma - Y$) increases to 1.80 eV in the ferroelectric phase and to 1.70 eV in the paraelectric one. Within HSE,

the crystal still has both the indirect and direct gap defined at the same points in the first Brillouin zone as within PBE, but the forbidden gap rises up to 2.30 eV and the direct gap

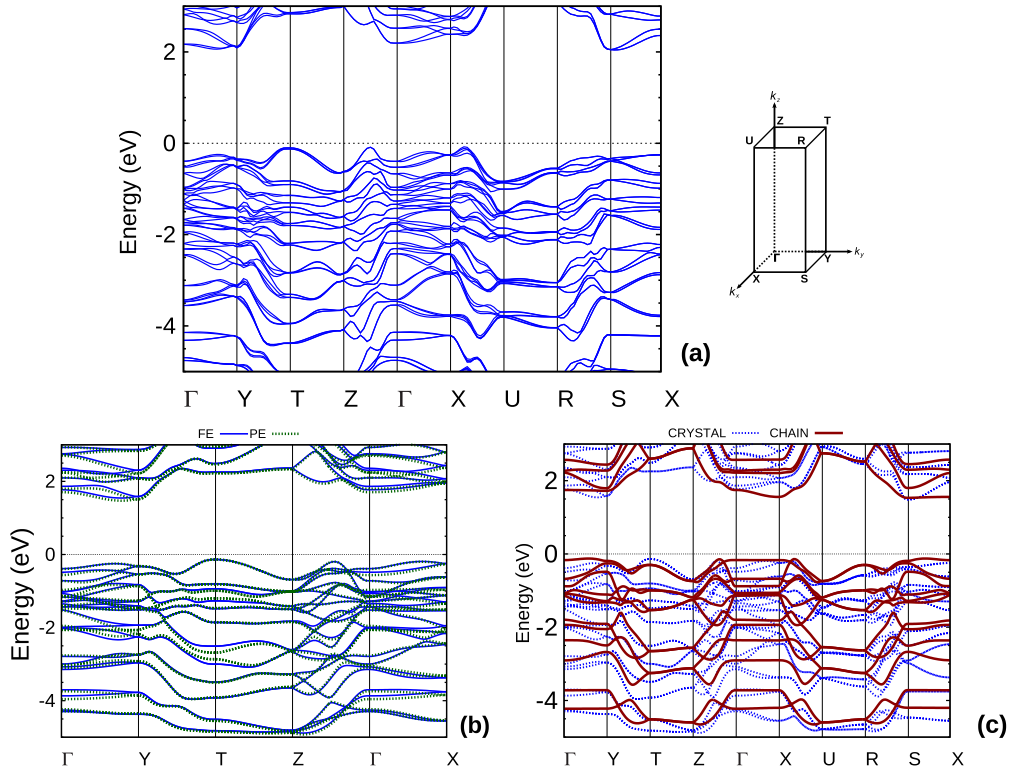


FIG. 3. (a) Band structure within HSE (SOC included) in the ferroelectric phase. The inset shows the Brillouin zone of the orthorhombic cell. (b) Comparison of band structure calculated for the paraelectric (PE) and ferroelectric (FE) phases by using PBE (no SOC). (c) Comparison between the band structure calculated in the FE SUC and on the full SbSI ferroelectric crystal, within PBE (no SOC).

up to 2.52 eV. For completeness, we compare the full band structures with and without FE displacements in Fig. 3(b), where the overall similarity of the paraelectric and ferroelectric electronic structure is evident.

Due to the presence of heavy elements, relevant effects are brought in by SOC. As shown in Fig. 3(a) (which refers to the ferroelectric phase), SOC acts to reduce the gap and to move the VBM of the indirect gap from the T point in the Brillouin zone to a point along the $X - U$ line, whereas the CBM stays in proximity to the S point. In the ferroelectric phase the indirect gap ($X - U \rightarrow S$) decreases to 2.15 eV, while the direct gap ($\Gamma - Y$) is about 2.30 eV. The calculated energy gap values are smaller than those observed in typical ferroelectric oxides (i.e., >3 eV in BaTiO₃; >4 eV in LiNbO₃) and are consistent with the (relatively wide-gap) semiconducting character of the compound of interest, as well as with previous studies [23]. The energy gap range is quite suitable for the proposed application of SbSI as a photoferroic material; it is also consistent with the experimental estimate $E_g \simeq 1.80$ eV [39,40] and with the proposed values of the absorption edges calculated by the empirical pseudopotential method [37] (1.82 eV and 2.0 eV for the paraelectric and the ferroelectric phases, respectively).

Finally, in order to discuss the band dispersion as a function of the investigated lines in the first Brillouin zone, a comparison between the band structure resulting from a single-double-chain characterizing the SUC and from the full SbSI crystal is useful. In Fig. 3(c), we report the results for the ferroelectric phase for both mentioned configurations. In reasonable agreement with the roughly one-dimensional chainlike character of the crystal, it is evident that the energy dispersion of $E_n(\mathbf{k})$ for Sb₃ - Sb₄ - S₃ - S₄ - I₁ - I₂ “double chain” is completely flat along the direction k_x perpendicular to the polarization direction on the reciprocal space, whereas the presence of an intrachain interaction along the b direction in real space affects the trend along k_y , especially for states in the upper valence bands; on the other hand, a relevant dispersion results along the k path parallel to k_z (such as along $Z - \Gamma$ or $X - U$). Even though similar considerations affect the band structure of the SbSI crystal, one can appreciate the effect of the interaction between the two double chains that gives rise to a sizable dispersion along both the directions in the planes perpendicular to the k_z axis.

Let’s now focus on the electron and hole effective masses in the SbSI crystal, m_e^* and m_h^* , respectively. The m_e^* has been calculated around the CBM at S point along the k_x , k_y , and k_z directions in the Brillouin zone, whereas the m_h^* has been calculated in the two distinct maxima of the valence band observable around T point and along the $X - U$ line (the absolute maximum within the SOC corrections). Moreover, we estimated both m_h^* and m_e^* in the valence and conduction bands along the $\Gamma - Y$ line, where we found the smallest direct band gap. The effective masses are reported in Table IV. The obtained electron and hole effective masses, estimated from the curvature of first-principles bands, obviously reflect the dispersion trend as a function of the k path in the Brillouin zone and give additional information about the mobility of the charge carriers in the crystal. For example, a much larger value is obtained along k_x , compared to k_y and especially k_z , leading to a larger anisotropy in the effective mass tensor. Indeed, the relatively small values of m^* at the VBM and CBM

TABLE IV. Electron- and hole-effective masses within PBE (SOC included) are reported in terms of m^*/m_e . The columns refer to the different directions in the Brillouin zone along which the estimate has been performed.

m_h^*					m_e^*			
T point		$X - U$	$\Gamma - Y$		S point			$\Gamma - Y$
k_x	k_y	k_z	k_z	k_y	k_x	k_y	k_z	k_y
1.30	0.40	0.7	0.38	0.46	1.30	0.40	0.20	0.43

of the indirect gap and the local maximum in the valence band and the corresponding local minimum in the conduction band, which define the optical band gap, suggest the possible use of SbSI in semiconductor devices.

V. FERROELECTRIC PROPERTIES

In order to gain insight into the ferroelectric behavior of SbSI, we compare the relaxed centric and polar structures shown in Fig. 1(c). When comparing the FE polarization within PBE and HSE (for the HSE-equilibrium geometry), the changes in the magnitude of polarization were found to be less than a few percent, confirming the validity of GGA to study the electronic and ferroelectric properties of SbSI (at fixed geometry), even though it fails in estimating the correct energetics of the system.

In order to have more insights, we built an adiabatic path from the PE to FE state by means of linear interpolation of the atomic coordinates, labeled with a generalized coordinate denoted as λ . In Fig. 4 we report the variation of the total energy from the centrosymmetric ($\lambda = 0$) to the noncentrosymmetric ($\lambda = \pm 1$) structures as a function of the amplitude of the polar mode. We found a bistable energy profile characteristic of a ferroelectric material, with an energy barrier of about 6 meV/unit cell. Regarding the polarization for SbSI, it lies along the c crystallographic direction, compatibly with the symmetry of the space group, with a calculated magnitude of $P \simeq 20 \mu\text{C}/\text{cm}^2$ both for PBE potential and HSE corrections, in good agreement with experimental measurements [18]. From Fig. 4 it is evident how polarization behaves almost linearly as a function of λ . This shows that, the FE polarization being the sum of an ionic and electronic contribution, the latter does not show any nonlinear effect, rather following the ionic contribution, which, by construction, linearly increases with atomic displacements.

Let’s now investigate more the nature of the electronic bonding system and its relation with ferroelectricity. Recalling that SbSI is characterized by a zigzag quasi-rhombic-bipyramidal arrangement chainlike along the crystallographic c axis, the atoms surrounding the antimony atom are arranged in nonsymmetrical coordination polyhedra and the antimony cation site does not show inversion symmetry (even in the paraelectric structure). This allows for the presence of active lone pair electrons $E(\text{Sb})$, which tends to occupy the region of space in between the chains. Although the lone pair is present already in the PE phase, its reorientation in going from the PE to the FE phase might play an active role in the stabilization of ferroelectricity, as discussed below. Indeed, a

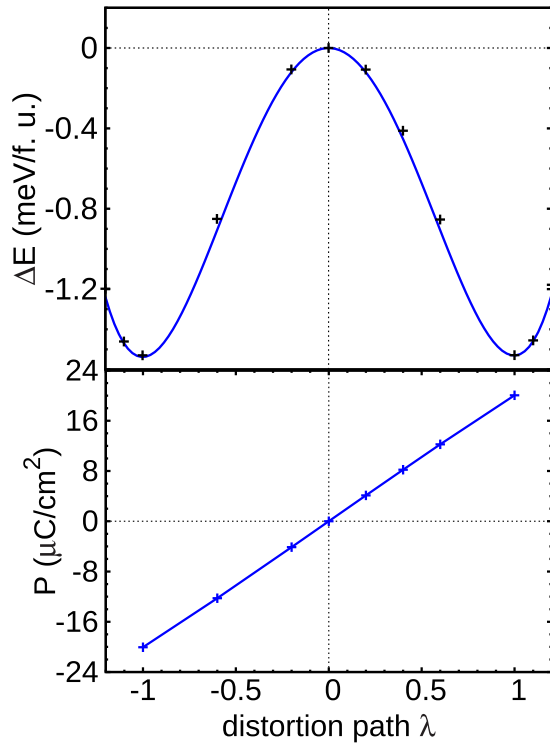


FIG. 4. Variation of HSE total energy (in meV/formula-unit, top) and polarization (in $\mu\text{C}/\text{cm}^2$, bottom) as a function of the amplitude of the polar distortion between centric ($\lambda = 0$) and polar ($\lambda = \pm 1$) configurations.

simple model for the electronic system in SbSI (both PE and FE phases) can be put forward [see Fig. 2(d)]. When considering the corresponding atomic orbital energies (as calculated by DFT and reported in Ref. [23]), we have the following: -17.3 I (s); -17.2 S (s); -12.7 eV Sb (s); -7.0 eV I (p); -6.9 eV S (p); -4.7 eV Sb (p). Although sulfur and iodine show almost the same atomic p energy levels, one can state that, due to the large halide electronegativity, iodine forms rather ionic bonds, whereas the covalent behavior mainly results from the hybridization between antimony and sulphur. The $s - p$

hybridization in antimony sulphoiodide is proved by the partial density of states, Figs. 2(a) and 2(b), and by the partial charge density in the valence band arising from strong interaction with anion S states (cf. Fig. 5): the considerable character of cation Sb s state in the upper part of the valence band can be ascribed to bonding and antibonding states. In turn, unoccupied cation p states hybridize with the antibonding states, resulting in an overall stabilization of the occupied electronic states, as shown in the simplified scheme in Fig. 2(d).

By performing the projection of the charge density on the lattice plane parallel to the height of the pyramid building block, we first note that the charge distribution is strongly affected by the polarity of the crystal [see charge density cuts shown in Figs. 5(a) and 5(b)]. In fact, between the paraelectric and the ferroelectric phases one can observe the slight change in the charge redistribution following the formation of the shorter bonds. In the energy range $[-2.0 : 0]$ eV, the presence of the $E(\text{Sb})$ lone pair is clear, according to the abundance of s orbital character in the l -decomposed DOS. In the ferroelectric phase, the lone-pair follows the distortion as a function of the polar mode $\lambda = \pm 1$, tilting towards the opposite direction with respect the greater bond angle, i.e., the shorter bond, along the polarization c direction. In Fig. 5(d), showing an isosurface from partial charge density in the energy range $[-2 : 0]$ eV for the FE phase, the lone pair is visible on top of Sb_3 and Sb_4 . The presence of the Sb lone pair is consistent with its location in the crystal, namely opposite to the pyramidal Sb-S bond and extending in the “empty” region between chains, so as to minimize the Coulomb repulsion with other bonding electrons. The high polarizability of the lone pairs, believed to be at the basis of the symmetry-lowering transitions in many FE materials (for example, BiFeO_3 [41]) is evident in the FE state, where the lone pairs are consistently arranged, so as to contribute, with their reorientation, to the stabilization of the FE phase. As in every displacive FE, the pairing distortion between Sb and S along the c direction, in the noncentrosymmetric structure, leads to energy lowering: the energy gain coming from the shortened Sb-S is larger than the energy loss from the lengthened Sb-S. This energy gain is higher when considering the interaction between a contracted with a diffused orbital, as it is the case between S $3p$ and

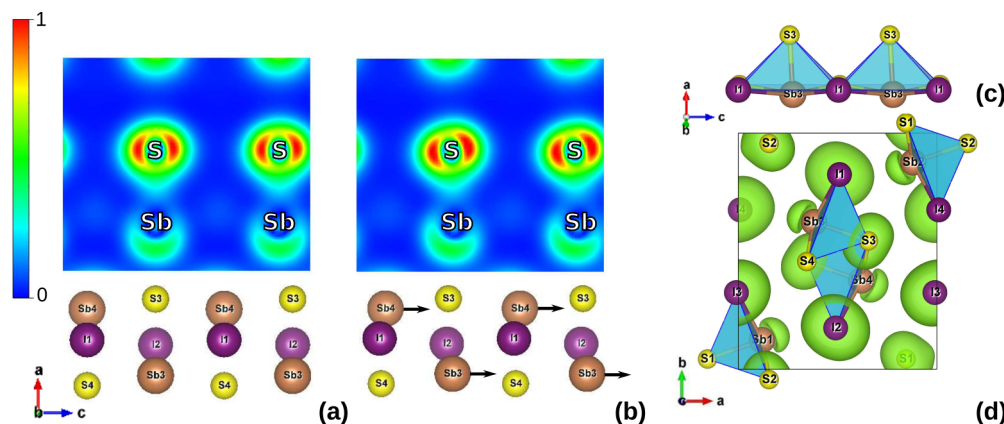


FIG. 5. Partial charge density (upper part) in the energy range $[-2 : 0]$ eV in both PE (a) and FE (b) phase, along with related ionic arrangements (bottom part). The Sb lone pair, $E(\text{Sb})$, is visible with a light green color in both phases. In the FE phase, the $E(\text{Sb})$ tilting has a net component along the polarization c axis and opposite to the Sb displacement. The charge distribution has been projected on the plane parallel to the pyramid’s height, Sb_3 - S_3 , as shown in panel (c). (d) Isosurface from partial charge density in the energy range $[-2 : 0]$ eV for the FE phase.

Sb 5s. As usual in ferroelectrics, any bond dimerization has to counteract the energy loss resulting from elastic energy. The delicate competition between the two terms is generally labeled as “second-order Jahn-Teller” effect [42,43]. Clearly, the lower total energy of FE vs PE states includes all the contributions and shows that dimerization finally wins. In a simplified view, however, some hints on the hybridization-driven gain can be inferred by the comparison of the P-DOS plots calculated for the S *p*-states of the paraelectric and ferroelectric structures, i.e., the structure without and with pairing distortion. We found in the upper of the valence band, [−6 : 0] eV, a slightly higher *p*-weight at lower energies as the result of pairing (not shown).

Further hints on the bond covalency can be gained by the calculated dimensionless “Born charge tensor” (or *dynamical charge*) [44]. In the extreme ionic limit, Born charges coincide with static charges of the ions, i.e., “nominal” values (Sb⁽³⁺⁾, S^(2−), and I^(1−)). As *z* is the polarization axis and considering that in the *x*-*y* plane the two double chains interact weakly one with the other, we focused on the diagonal component of the dynamical charge tensor along the *z* direction. Our calculations show that the transversal components of $Z^{*(T)}$ are +6.7, −3.7, −3.0 in the ferroelectric phase and +7.1, −3.9, −3.2 in the paraelectric phase, therefore substantially deviating from the amplitude of the nominal ionic charges. As expected from the relevant mixing of the orbital characters in the density of valence states [cf. Figs. 2(a) and 2(b)] and the kind of hybridization at the basis of the electronic system, the significant deviations of the dynamical charges with respect to the nominal ones involve mostly the *active* Sb, but also S and I atoms.

This behavior can be better clarified by describing the atomic distortion from the paraelectric to the ferroelectric phase as a cooperative motion around the center of mass (c.m.) of the system, i.e., by keeping the center of mass fixed (rather than fixing the I atom). Within this framework, the c.m. is located at 2.08 Å and at 2.17 Å in the paraelectric and ferroelectric structure, respectively, and the related atomic displacements are $\tau_{Sb}^{c.m.} = +0.10$ Å, $\tau_S^{c.m.} = -0.04$ Å, and $\tau_I^{c.m.} = -0.08$ Å. This allows one to better point out the important role of Sb, which mostly contributes to the polarization because of its largest $Z^{*(T)}$, and the displacive ferroelectricity, due to the opposite motion of the (I, S) anions and (Sb) cation. Moreover, it also confirms the mixed ionic and covalent character of the bonds, common to many well-known ferroelectrics.

VI. INTERPLAY BETWEEN FERROELECTRICITY AND SPIN-ORBIT COUPLING

As already discussed, the cooperative atomic motion along the crystallographic *c* axis leads to FE polarization and, by construction, a reversal of the latter is obtained when switching the polar mode (i.e., $\lambda = \pm 1$). Now, we examine if Dresselhaus and Rashba effects arise due to SOC and FE polarization and, if so, how they depend on the atomic displacements. As clearly visible in Figs. 6(a) and 6(b), the valence and conduction bands (otherwise twofold degenerate in the absence of SOC) are spin-split along several BZ symmetry lines. Looking at the band dispersion, we see that, despite the SOC splitting, the lines around the conduction band minimum (CBM) *S* are still twofold degenerate (as they arise from equivalent sublattices

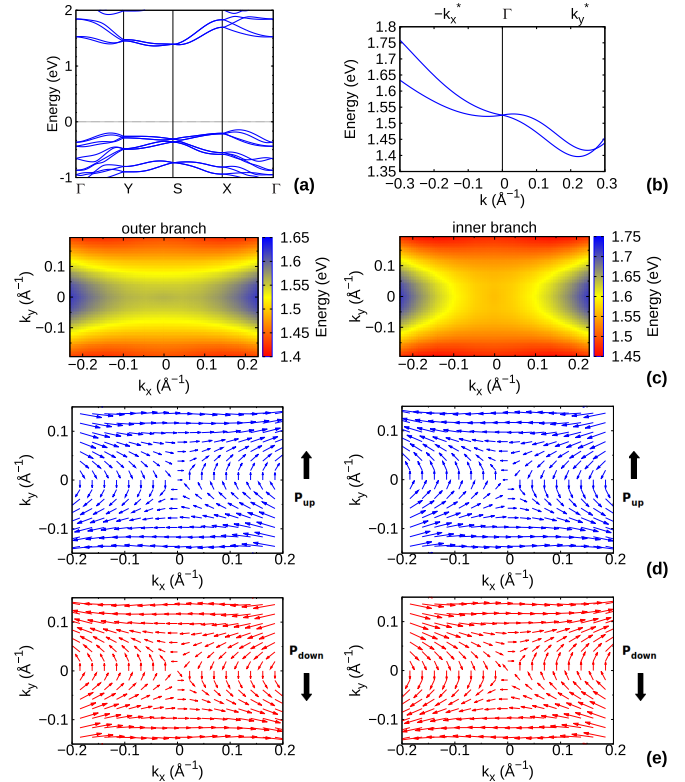


FIG. 6. (a) PBE band dispersion along symmetry lines in the plane perpendicular to k_z^* and (b) a zoom of the conduction band around the Γ point along $\Gamma - X$ and $\Gamma - Y$ lines. (c) PBE energy profiles around Γ of the two lowest conduction bands (called outer and inner branches). Related spin texture as a function of the ferroelectric polarization: (d) + \mathbf{P} (blue) and (e) − \mathbf{P} (red). In all panels, k_x^* and k_y^* span a plane perpendicular to the polarization direction.

in the crystalline unit cell), whereas they are split around Γ . Therefore, driven by the simpler situation at the Brillouin zone center from the symmetry point of view, we decided to focus on the spin texture of the conduction bands along the $k_x^*(\Gamma - X)$ and the $k_y^*(\Gamma - Y)$ directions perpendicular to the FE polarization. In this case the energy splittings around Γ , corresponding to the difference of the energy band extrema between the inner and the outer branches, are $\simeq 22$ meV along the k_y^* and $\simeq 7.5$ meV along the k_x^* directions (the energy spin splitting values for the corresponding valence band are much smaller, i.e., $\simeq 8.6$ meV along the k_x^* and $\simeq 0.5$ meV along the k_y^*). However, the different orbital hybridization at play leads to a complex nonparabolic band structure. The outer and inner branches of the spin-split conduction bands show two dissimilar trends along the k_x^* and k_y^* directions due to differences between the effective masses along the two directions, Γ being a saddle point [cf. Fig. 6(b)]. These two split bands present nontrivial and opposite spin textures, with spin orthogonal to the crystal momenta along the k_x^* and k_y^* axes, but radial along the diagonal directions, as shown in Figs. 6(c) and 6(d).

Despite the complex band structure around Γ , one can still resort to a $\mathbf{k} \cdot \mathbf{p}$ Hamiltonian modeling, already proposed for different materials (i.e., hybrid perovskite-halides) but showing similar symmetry properties as far as spin splitting is concerned [5]. Indeed, the SOC-induced band splitting around

Γ point can be understood by inspecting the symmetries allowed in the $\mathbf{k} \cdot \mathbf{p}$ Hamiltonian around that point. Since the Γ point preserves time-reversal symmetry, a ‘‘Kramer pair’’ is observed. The point-group symmetry at Γ in the FE phase is C_{2v} . Looking at the linearity of H_{SO} as a function of the \mathbf{k} vector and by introducing the considered symmetries in SbSI, the SOC-induced term takes the form $-\alpha k_x^* \sigma_y + \beta k_y^* \sigma_x$, where α and β denote material-dependent constants. By writing down the SOC term in the local reference system it is possible to highlight both Rashba and Dresselhaus linear terms; we obtain $\alpha_R(-k_x^* \sigma_y + k_y^* \sigma_x) + \alpha_D(-k_x^* \sigma_x + k_y^* \sigma_y)$, where the first (second) linear term describes the Rashba (Dresselhaus) effect. The coupling constants are defined as $\alpha_R = (\frac{\alpha+\beta}{2})$ and $\alpha_D = (\frac{\alpha-\beta}{2})$. By adding to the ordinary quadratic term involving effective masses, $\frac{\hbar^2 k^2}{2m^*}$, this Rashba-Dresselhaus spin-splitting correction and by fitting of the two conduction bands shown in Fig. 6(b) along k_x^* and k_y^* directions, we found that around Γ the Rashba and Dresselhaus coupling coefficients amount to $\alpha_R = 0.055$ eV \AA and $\alpha_D = 0.205$ eV \AA , respectively. This shows that the Dresselhaus coupling is present and dominates over the Rashba-like term, thus explaining the origin of spin textures in SbSI.

Since the bulk Rashba α_R and Dresselhaus α_D constants strongly depend on the potential gradient around the ferroelectrically active ions, it is possible to anticipate changes in the spin texture depending on both the direction and sense of FE polarization. In particular, the switching of polarization via the application of an external field along z is expected to lead to a reversal of the spin texture [5,9]. In Figs. 6(c) and 6(d), indeed, we show that the Dresselhaus-like spin textures are reversed by going from $-\mathbf{P}$ to $+\mathbf{P}$ in the FE structure, with typical spin switching between the inner and outer branch. Within this framework, as the Rashba-Dresselhaus spin texture is tightly linked to the polarization direction and, therefore, electrically tunable, the polarization in SbSI opens interesting perspectives in spintronics [9,15]: the possibility to switch the direction of polarization via an electric field implies a corresponding control over the spin degrees of freedom and new ways to exploit these effects in photovoltaics by involving lead-free materials.

VII. CONCLUSIONS

In this work we have presented a comprehensive study of structural, electronic and ferroelectric properties of the ferroelectric semiconductor antimony sulfoiodide (SbSI), by means of first-principles DFT-based calculations. We found that standard DFT (using either PBE or LDA, with or without

SOC, including or not Grimme’s correction for van der Waals interactions) fails in reproducing the experimentally observed ferroelectric phase, predicting the paraelectric structure as the stable one. On the other hand, a more advanced approach, based on hybrid functionals, correctly leads to the cooperative atomic displacements along the z axis, i.e., displacive ferroelectricity. However, once the atomic positions are fixed to those predicted by HSE, the standard PBE density functional still provides a good description of the electronic and ferroelectric properties. Focusing on the band structure calculated within the HSE functional including SOC, in the ferroelectric phase, the forbidden gap amounts to 2.15 eV, whereas the smallest direct gap along the $\Gamma - Y$ line is about 2.30 eV. The optical energy gap range is quite consistent with the spectral region suggested for photovoltaic devices. The calculated spontaneous polarization of $P \simeq 20$ $\mu\text{C}/\text{cm}^2$ and a bistable energy profile with an energy barrier of about 6 meV/unit cell unambiguously characterize the ferroelectric behavior of SbSI. In order to shed light on ferroelectricity of antimony sulfoiodide, we analyzed the transition phase in terms of chemical bonding character and charge distribution. From the SbSI partial charge density it emerges that a Sb lone pair is clearly visible in the valence band, occupying, in both the PE and FE phases, the region in between the zigzag chains. The high polarizability of the lone pair likely contributes to FE stabilization, as a tilting of the lone pair is observed as a function of the polar distortions. As expected from the relevant mixing of the orbital characters in the density of valence states and the kind of hybridizations at the basis of the electronic system, the Born effective charge associated to the (active) Sb, S, and I atoms (+6.7, -3.7, and -3.0, respectively), considerably deviate with respect to the nominal charges. Finally, we focused on the spin texture of the conduction bands along the $k_x^*(\Gamma - X)$ and the $k_y^*(\Gamma - Y)$ directions perpendicular to the FE polarization. We found that, when FE polarization is switched from P to $-P$, the spin textures are fully reversed and, moreover, that the coexistence of Rashba and Dresselhaus relativistic effects are allowed in SbSI crystal, with possible perspectives in spintronics.

ACKNOWLEDGMENTS

We gratefully acknowledge many useful discussions with Dr. Domenico Di Sante, Dr. Alessandro Stroppa, Dr. Emilie Bruyer, and Dr. Paolo Barone. D.A. would like to thank Professor Philippe Ghosez for interesting discussions. Figures have been produced by using VESTA package [45].

-
- [1] *Physics of Ferroelectrics: A Modern Perspective*, edited by K. M. Rabe, C. H. Ahn, and J.-M. Triscone (Springer, Berlin, 2007), Vol. 105.
 - [2] E. I. Rashba, *Sov. Phys. Solid. State* **2**, 1109 (1960).
 - [3] R. Winkler, *Spin-Orbit Coupling Effects in Two-Dimensional Electron and Hole Systems* (Springer-Verlag, Berlin, 2003).
 - [4] S. M. Young and A. M. Rappe, *Phys. Rev. Lett.* **109**, 116601 (2012).
 - [5] A. Stroppa, D. Di Sante, P. Barone, M. Bokdam, G. Kresse, C. Franchini, M.-H. Whangbo, and S. Picozzi, *Nat. Commun.* **5**, 5900 (2014).
 - [6] P. Gambardella and I. M. Miron, *Philos. Trans. R. Soc. London A* **369**, 3175 (2011).
 - [7] G. Dresselhaus, *Phys. Rev.* **100**, 580 (1955).
 - [8] K. Ishizaka *et al.*, *Nat. Mater.* **10**, 521 (2011); A. Crepaldi, L. Moreschini, G. Autes, C. Tournier-Colletta, S. Moser, N. Virk, H. Berger, P. Bugnon, Y. J. Chang, K. Kern, A. Bostwick,

- E. Rotenberg, O. V. Yazyev, and M. Grioni, *Phys. Rev. Lett.* **109**, 096803 (2012).
- [9] D. Di Sante, P. Barone, R. Bertacco, and S. Picozzi, *Adv. Mater.* **25**, 509 (2013).
- [10] X. Zhang, Q. Liu, J.-W. Luo, A. J. Freeman, and A. Zunger, *Nat. Phys.* **10**, 387 (2014).
- [11] S. Picozzi, *Front. Phys.* **2**, 10 (2014).
- [12] E. Plekhanov, P. Barone, D. Di Sante, and S. Picozzi, *Phys. Rev. B* **90**, 161108(R) (2014).
- [13] D. Di Sante, P. Barone, E. Plekhanov, S. Ciuchi, and S. Picozzi, *Sci. Rep.* **5**, 11285 (2015).
- [14] M. Kepenekian, R. Robles, C. Katan, D. Saponi, L. Pedesseau, and J. Even, *ACS Nano* **9**, 11557 (2015).
- [15] M. Kim, A. J. Freeman, J. Ihm, and H. Jin, *Proc. Natl. Acad. Sci. USA* **111**, 6900 (2014).
- [16] A. Narayan, *Phys. Rev. B* **92**, 220101(R) (2015).
- [17] R. Nietsche and W. J. Merz, *J. Phys. Chem. Solids* **13**, 154 (1960).
- [18] E. Fatuzzo, G. Harbeke, W. J. Merz, R. Nietsche, H. Roetschi, and W. Ruppel, *Phys. Rev.* **127**, 2036 (1962).
- [19] D. Berlincourt, H. Jaffe, W. J. Merz, and R. Nietsche, *Appl. Phys. Lett.* **4**, 61 (1964).
- [20] R. Kern, *J. Phys. Chem. Solids* **24**, 957 (1963).
- [21] A. Audzijonis *et al.*, *Ferroelectrics* **219**, 37 (1998).
- [22] A. Audzijonis *et al.*, *Solid State Commun.* **147**, 88 (2008).
- [23] K. T. Butler, J. M. Frost, and A. Walsh, *Energy Environ. Sci.* **8**, 838 (2015).
- [24] T. Inushima, *J. Phys. Chem. Solids* **60**, 587 (1999).
- [25] VASP official website: <http://cms.mpi.univie.ac.at/vasp>
- [26] G. Kresse and J. Furthmüller, *Phys. Rev. B* **54**, 11169 (1996).
- [27] J. P. Perdew, K. Burke, and M. Ernzerhof, *Phys. Rev. Lett.* **77**, 3865 (1996).
- [28] J. Heyd, G. Scuseria, and M. Ernzerhof, *J. Chem. Phys.* **118**, 8207 (2003).
- [29] W. Kohn and L. Sham, *Phys. Rev.* **140**, A1133 (1965).
- [30] S. Grimme, *J. Comput. Chem.* **25**, 1463 (2004).
- [31] R. D. King-Smith and D. Vanderbilt, *Phys. Rev. B* **47**, 1651 (1993).
- [32] A. Kikuchi, Y. Oka, and E. Sawaguchi, *J. Phys. Soc. Jpn.* **23**, 337 (1967).
- [33] E. Dönges, *Z. Anorg. Allg. Chem.* **263**, 112 (1950).
- [34] E. Furman, O. Brafman, and J. Makovsky, *Phys. Rev. B* **13**, 1703 (1974).
- [35] A. Audzijonis *et al.*, *Physica B* **391**, 22 (2007).
- [36] R. Blinc, M. Mali, and A. Novak, *Solid State Commun.* **6**, 327 (1968).
- [37] K. Nako and M. Balkanski, *Phys. Rev. B* **8**, 5759 (1973).
- [38] By performing a symmetry analysis of the GGA/LDA optimized geometry with the STRCONVERT tool, of the Bilbao Crystallographic Server, the centrosymmetric *Pnam* space group is obtained; for the sake of restoring an inversion center, the symmetry tool brings back *z* coordinates from 0.270 to 0.250, considering a 0.001 tolerance.
- [39] P. Szperlich *et al.*, *Mater. Sci-Poland* **32**, 669 (2014).
- [40] V. M. Fridkin, *Ferroelectrics-Semiconductors* (Nauka, Moscow 1976), p. 408.
- [41] R. Seshadri and N. A. Hill, *Chem. Mater.* **13**, 2892 (2001).
- [42] I. B. Bersuker, *Chem. Rev.* **101**, 1067 (2001).
- [43] I. B. Bersuker, *The Jahn-Teller Effect and Vibronic Interactions in Modern Chemistry* (Plenum, New York, 1984).
- [44] P. Ghosez, J.-P. Michenaud, and X. Gonze, *Phys. Rev. B* **58**, 6224 (1998).
- [45] K. Momma and F. Izumi, *J. Appl. Crystallogr.* **44**, 1272 (2011).